Analyst

ROYAL SOCIETY OF CHEMISTRY

PAPER

View Article Online
View Journal | View Issue

Cite this: *Analyst*, 2022, **147**, 1117

A modular microfluidic platform for serial enrichment and harvest of pure extracellular vesicles†

Hogyeong Gwak, [a] Sunyoung Park, [a] Haeun Yu,[a] Kyung-A. Hyun *[a] and Hyo-Il Jung *[a,b]

Extracellular vesicles (EVs) are recognized as promising biomarkers for several diseases. However, their conventional isolation methods have several drawbacks, such as poor yields, low purity, and time-consuming operations. Therefore, a simple, low-cost, and rapid microfluidic platform has been extensively developed to meet the requirement in biomedical applications. Herein, a modular microfluidic platform is demonstrated to isolate and enrich EVs directly from plasma, in a combination of continuous capture and purification of EVs. The EVs were selectively captured by target-specific antibody-coated beads in a horseshoe-shaped orifice micromixer (HOMM) chip within 2 min. A fish-trap-shaped microfilter unit was subsequently used to elute and purify the affinity-induced captured EVs from the microbeads. The ability of the modular chip to capture, enrich, and release EVs was demonstrated in 5 min (100 μL sample) at high throughput (100 μL min^{-1}). The two chips can be modularized or individually operated, depending on the clinical applications such as diagnostics and therapeutics. For the diagnostic applications, the EVs on microbeads can be directly subjected to the molecular analysis whereas the pure EVs should be released from the microbeads for the therapeutic treatments. This study reveals that the fabricated modular chip can be appropriately employed as a platform for EV-related research tools.

Received 7th December 2021,
Accepted 20th February 2022

DOI: 10.1039/d1an02220b

rsc.li/analyst

1. Introduction

Extracellular vesicles (EVs) are nanometer-sized lipid bilayer vesicles released by all cells in both eukaryotes and prokaryotes. EVs carry various biomarkers, including DNA, RNA, lipids, metabolites, and cytosolic and cell surface proteins, depending on their origin, and play a crucial role in the bidirectional communication between cells and their microenvironment.[1–4]

Research on EVs has been conducted in the medical field as potential diagnostic, prognostic, and predictive biomarkers for many years.[5] Tumor-derived EVs (TDEs) have an effect on promoting cancer proliferation, invasion, progression, metastasis, remodeling, and drug resistance in the tumor microenvironment[5–7] and in addition, TDEs and their cargo are highly specific for cancer cells as they reflect the characteristics of their origin.[8,9] EVs can be detected from several types of tumors such as Lung, Pancreatic, prostate, breast, and ovarian cancer, *etc.*[10] Consequently, research on EVs has focussed on leveraging the potential of these diagnostic biomarkers and therapeutic substances to combat various diseases.[11–14]

Because EVs are surrounded by diverse biomarkers in all biological fluids, the practical application of EVs in rigorous biochemical assays for clinical purposes requires their enrichment and purification from other non-EV components.[15] Popular label-free isolation methods for EVs, such as membrane filtration, size-exclusion chromatography (SEC), ultracentrifugation (UC), and differential ultracentrifugation (dUC), have several drawbacks such as low yield, time-consuming processes, and poor selectivity for disease-associated EVs.[15–18] To overcome the limitations of the aforementioned size- and density-based methods, affinity-based purification methods were conducted using tetraspanins (such as CD9, CD81, and CD63, which are commonly used as EV markers) or surface protein markers of disease-related cells have been exploited. However, it has certain disadvantages such as tedious processes (binding, washing, and elution), low purification, long operational duration, and poor yields.[19–21]

Microfluidic devices show tremendous promise as medical diagnostic tools. Microfluidic technology enables continuous flow and engineered environments for molecular reactions,

[a]*School of Mechanical Engineering, Yonsei University, Seoul, 03722, Republic of Korea. E-mail: hyunkkuplus@gmail.com, uridle7@yonsei.ac.kr*
[b]*The DABOM Inc., Republic of Korea. E-mail: uridle7@yonsei.ac.kr*

†Electronic supplementary information (ESI) available. See DOI: 10.1039/d1an02220b

resulting in less restrictive sample volumes, short experimental durations, high throughput, high efficiency, and high selectivity compared to those of batch procedures.[8,22–32]

Previous studies regarding immunoaffinity-based microfluidic platforms have been performed in the low flow rate range to induce sufficient antigen–antibody interactions. In order to increase the capture efficiency of EVs in a rapid manner, it was designed that patterned microfluidic channel structures and nanowires embedded in microfluidic chips, however, the fabrication steps are complicated, and the cost is high.[24,30,31]

Therefore, a modular microfluidic platform was developed in this study to enrich EVs on micron-sized carrier beads immobilized with EV-specific antibodies, based on affinity capture, and elute pure EVs from the carrier beads in a high throughput. The modular microfluidic platform consists of two microfluidic chips: a horseshoe-shaped orifice micromixer (HOMM) unit and a fish-trap-shaped microfilter unit (fish trap). The HOMM chip permits effective collisions between the EVs and phenotype-related antibody-coated carrier beads for rapid immune-affinity-based immobilization of EVs onto the carrier beads. Subsequently, these EV-carrying carrier beads are trapped by the hydrodynamic filter structure in the fish trap chip. Finally, upon the injection of the elution buffer, only pure EVs are eluted out of the chip while the carrier beads remain captured.

2. Experimental

2.1. Fabrication of the modular microfluidic platform

The modular microfluidic platform consists of two microfluidic chips: a HOMM chip and a fish trap chip. Conventional soft lithography techniques were used to fabricate two chips. To fabricate the mold for the polydimethylsiloxane (PDMS) device, a negative photoresist (SU-8 3035, MicroChem Corp., USA) was patterned on a silicon wafer. The two fabricated molds were employed to construct the microfluidic channels. The PDMS channels replicated from the mold and slide glass were bonded *via* oxygen plasma treatment. The detailed information about the whole procedure can be found in our previous report.[8]

2.2. Preparation of antibody-coated beads and EVs

To immobilize antibodies on the microbead surfaces, 5 μg of biotinylated anti-CD63 antibodies (ab134331; Abcam, UK) were mixed with 1 mg of streptavidin-coated polystyrene microbeads (SVP-60-5; Spherotech, USA). The mixture was incubated for 30 min at room temperature (23 °C) using a rotator. Breast cancer cell MDA-MB-231 and Jurkat cells were purchased from the Korean Cell Bank. All of cells were grown in an RPMI-1640 medium (Cellgro, USA) supplemented with 10% (v/v) fetal bovine serum (FBS; Gibco, USA) and 1% (v/v) penicillin–streptomycin. The condition of incubation was performed in a humidified atmosphere of 5% CO_2 at 37 °C. Once the cells were grown to a confluence of 80%–90%, the cell surfaces were washed twice with serum-free media and incubated with a minimal volume of serum-depleted media to cover the cells. After 48 h of incubation, the cell culture media were collected and centrifuged at 2000*g* for 20 min and passed through 0.22 μm filters to remove large protein aggregates and other cellular debris. EVs were concentrated from the filtered cell culture media using a 100 K Macrosep advance centrifugal device, and subsequently stored at −80 °C until further use. Plasma samples from healthy controls were obtained from the Yonsei Severance Hospital. Plasma samples were obtained under the repository's Institutional Review Board-approved protocol (IRB number of Severance Hospital, Yonsei University: 4-2020-0350). The samples were stored at −80 °C prior to use.

2.3. Quantification of EVs

EVs were measured by nanoparticle tracking analysis system (NTA; Nanosight LM10, Malvern Panalytical, UK), which can differentiate size distribution and concentration of nanoparticles in a liquid. Ten-second-long videos were captured at 30 frames per s, and the movement of EVs was analyzed using NTA software (NanoSight NTA 3.2). The experiments were repeated at least three times to obtain representative results.

The EVs bound to the microbeads passing through the microfluidic chip were investigated by flow cytometry. The EVs bound to the microbeads were fluorescently labeled with the CD63-PE-Cy7 antibody for 30 min at room temperature. After washing twice with FACS buffer (PBS containing 1% BSA and 0.1% NaN_3 (sodium azide)), fluorescence detection was performed immediately using the LSR II flow cytometer (BD, USA). Samples were analyzed until 10 000 events of microbeads were acquired. Gates were established to discriminate between doublet and small-sized debris using forward scatter and side scatter.

2.4. Assay of cellular uptake of EVs

To track EVs in cells, MDA-MB-231 cells were stained with 3 μM PKH67 dye in Diluent C (Sigma) in a final volume of 500 μL for 10 min at room temperature. Centrifugation was performed for 5 min at 600*g* with the addition of FBS-containing media to thoroughly wash the sample and remove the unbound dye. Subsequently, the PKH67-labeled EVs from the cells were mixed with either CD63 or Programmed death-ligand1 (PD-L1) antibody-coated microbeads using the microfluidic chip, and the captured EVs on the microbeads were rigorously isolated by the elution buffer thereafter. Captured EVs were released by the elution buffer (0.1 M glycine–HCl (pH 3)) and neutralised at pH 7.4 by using 1 M Tris–HCl (pH 9.0). Recipient cell lines were seeded at 60% confluence in a 6-well plate for 24 h under standard culture conditions at 37 °C. Standard media were replaced with FBS-free media prior to EV co-culture. A total of 10^7 particles of PKH67-labeled CD63 and PD-L1 EVs were administered to the cells. After the co-culture, the cells were concentrated to approximately one million cells per 50 μL for flow cytometry.

3. Results and discussion

3.1. Operational mechanism of the fabricated modular microfluidic platform

The strategy employed for enriching and harvesting EVs consists of three functional components: (1) immobilization of EVs onto carrier beads; (2–1) trapping of the EV-containing carrier beads; and (2–2) elution of pure EVs from the trapped carrier beads. In the immobilization step, EVs bind to the surfaces of anti-CD63 antibody-conjugated carrier beads. Moreover, all EVs must be labeled with PKH-67 dye to visualize and quantify them. During the harvesting stage of pure EVs involving injection of the elution buffer, the trapping step must ensure that the carrier beads are retained to guarantee that the harvested EVs are not contaminated with carrier beads.

A microfluidic platform was developed to accomplish the aforementioned strategy in a simple and timely manner (Fig. 1). Specifically, the microfluidic platform was modularized into two key microfluidic channels: (1) the HOMM channel for twisting the microfluidic flow and mixing the EVs and antibody-coated carrier beads, and (2) a microfiltration channel for trapping the EV-containing carrier beads and eluting pure EVs.

The HOMM channel increases the collisions between the EVs and carrier beads, enabling effective and continuous immobilization of EVs onto the bead surfaces within a short duration. Conventional micromixer channels induce the alignment of microbeads at a high Reynolds number (Re), which disrupts collisions between the microbeads and nanoparticles.

In contrast, the HOMM channel diminishes the microbead alignment in the channel at a high Re. The EV-containing carrier beads subsequently move into the fish trap unit connected to the HOMM channel for continuous capture, with the beads being greater in size than the gaps in the fish-trap-shaped filter structure.

Because the unit structure of the filter is loaded with beads, the leftover beads move to the subsequent structure. Carrier beads are concentrated in the filter structure. Subsequently, the elution buffer is injected into the fish trap chip, and pure EVs flow through the chip outlet. A photographic image and the dimensions of the microfluidic platform are shown in Fig. S1a and Fig. S1b,† respectively.

3.2. Design of the modular microfluidic platform

The front module is a micromixer that can quickly and efficiently isolate EVs. Efficient micromixer operation at high Re is a prerequisite for adhering the EVs to the carrier beads because conventional mixer designs based on straight channels encounter issues related to insufficient mixing efficiency under high Re conditions, enabling high throughput. Additionally, the mixing of EVs (nanoparticles) and antibody-

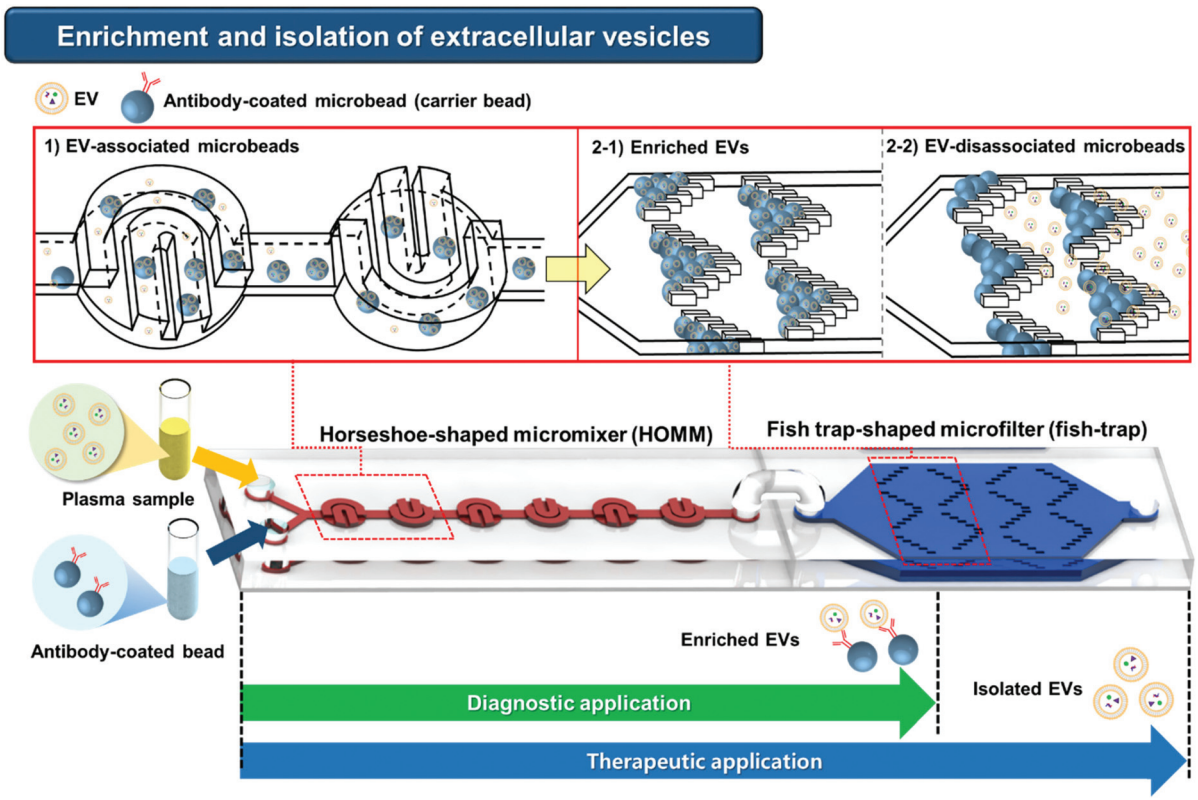

Fig. 1 Schematic illustrations of the designed modular microfluidic chip. (1) Horseshoe-shaped orifice micromixer (HOMM) channel for enhancing the collisions between antibody-coated beads and EVs to immobilse the EVs onto the beads. A fish-trap-shaped microfilter (fish trap) for (2–1) enrichment of the EV-containing carrier beads and (2–2) EVs isolated from the beads.

coated microbeads in a microfluidic channel at high flow rates is difficult. Therefore, a novel micromixer (HOMM) was designed in this study to achieve high-throughput binding of EVs and antibody-coated microbeads. In the micromixer module, the antigen–antibody reaction time can be reduced by the structure of the HOMM to increase the number of collisions between the nanosized EVs and micron-sized carrier beads.

Therefore, three types of channel structures were investigated to compare the factors influencing the mixing performance and to determine the optimal channel structure for strong coupling between the EVs and carrier beads (Fig. 2a). The first design, known as an orifice channel (OC), leads to a sudden expansion of the fluid in the horizontal plane. Moreover, a cylindrical orifice channel (COC) was designed to create a sudden expansion of the fluid in both the vertical and horizontal planes. Finally, the HOMM channel with two high horseshoe-shaped structures on top of a shallow circular orifice structure was devised. Computational fluid dynamics (CFD) simulations were performed to predict particle trajectories in the microfluidic channels with respect to streamlines, velocity vectors, fluid mixing, and particle movements (COMSOL Multiphysics 5.0). At a high Re (>25), the streamlines of the HOMM channel were adequately mixed in the horseshoe structure, indicating even distribution over the entire channel area. However, the streamlines in the OC system flowed along the initial streamline without mixing, and those in the COC system created vortices in the extended channel (Fig. 2b and Fig. S2†).

The flow velocity vector was simulated to analyze the magnitude and direction of the fluid flow (Fig. 2c). The fluid spread uniformly in the expansion channel in the OC, and was concentrated in the centre in the COC. However, the direction of the fluid changed along the two horseshoe channels in the HOMM. Therefore, analysis of the fluid flow vector indicates that the fluid moved adequately along the horseshoe channel. In addition, two different fluids were injected into inlet 1 (1 mol m^{-3}, red) and inlet 2 (0 mol m^{-3}, blue) along the channel length in all the geometries (Fig. 2d). When the two fluids were thoroughly mixed in the channels, the differently colored fluids (blue and red) intermingled to form a green-colored version (0.5 mol m^{-3}).

The two fluids were not perfectly mixed in cycle 1 in all the examined channels, which led to the presence of fluids in various colors. However, the color variations diminished with increasing number of cycles, and the fluid transformed into a green-colored version in the COC and HOMM, indicating the occurrence of mixing. In contrast, a fluid with several colors remained in the OC, indicating insufficient mixing (Fig. 2d). Additionally, trajectories of 200 nm-sized particles were analyzed at the *Y–Z* plane section from 0 s to 0.02 s at 0.004 s intervals to predict particle collisions (Fig. 2e). In both the OC and COC, particles were scattered in the direction of the expansion channel but were not mixed with each other. In contrast, the particles started mixing in the HOMM channel after 0.004 s owing to the transverse flow. Therefore, the HOMM channel was determined to be optimal for increasing the number of collisions between the carrier beads and EVs.

3.3. Validation of HOMM channel performance

One cycle of the HOMM operation led to a change in the fluid direction in the horseshoe-shaped structure. Therefore, the up- and down-mixing of the flow was analyzed for n cycles (Fig. 3a).

Additionally, the mixing performance of the chip was evaluated through particle mixing experiments and quantitatively analyzed. This can assist in describing parameters that display the effects of productive collisions between two particles, such as the EVs and antibody-coated microbeads. Two types of fluorescent beads were injected into each inlet of the HOMM to evaluate the mixing index (MI) between the EVs and antibody-coated microbeads. The flow was adjusted to a range of 25–200 μL min^{-1} using a syringe pump (KDS210, KDS Scientific Inc., USA). First, an experiment involving mixing of the two particles was conducted to determine the possible influence of the number of cycles and flow rate on the mixing efficiency. The mixing performance of the HOMM chip for 1, 50, 100, 150, and 200 cycles were quantitatively analyzed using the ImageJ program (NIH, USA), and the corresponding MIs were determined by measuring the pixel intensities in the color images (cycle section in Fig. 3a). The blue and green colors (representing 100 nm-sized and 7 μm-sized particles, respectively) transformed into a cyan color, indicating adequate mixing of the two particles, with increasing number of cycles increased (Fig. 3b). MI was estimated using the standard deviation (σ) of the pixel intensities, which was calculated as follows:

$$\sigma = \sqrt{\frac{1}{N}\sum_{i=1}^{N}(I_i - I_{max})^2}$$

here N is the number of pixels in the mixing area, I_i is the local pixel intensity, and I_{max} is the maximum pixel intensity in the mixing area.[33] MI was estimated as follows:

$$MI = 1 - \frac{\sigma_{cycle\ n}}{\sigma_{max}}$$

where $\sigma_{cycle\ n}$ is the standard deviation of cycle n, and σ_{max} is the maximum standard deviation in the HOMM.[8,33–35] MI represents the mixing of two differently colored beads inside the channel and ranges from zero (unmixed) to one (completely mixed). As shown in Fig. 3c, MI reached 0.8 at flow rates over 50 μL min^{-1} and when the number of cycles was between 100 and 150. The two particles were insufficiently mixed between cycles 1 and 50 at all flow rates. Moreover, MI decreased when the flow rate exceeded 200 μL min^{-1} and the number of cycles was over 200. Microbeads tend to be focussed and aligned by inertial forces when the hydrodynamical flow rate increases.

Second, a binding experiment between EVs and microbeads was conducted to confirm their collision. Based on the MI results of the HOMM chip, the number of cycles was adjusted to 50, and an operational flow rate of 50 μL min^{-1} was used.

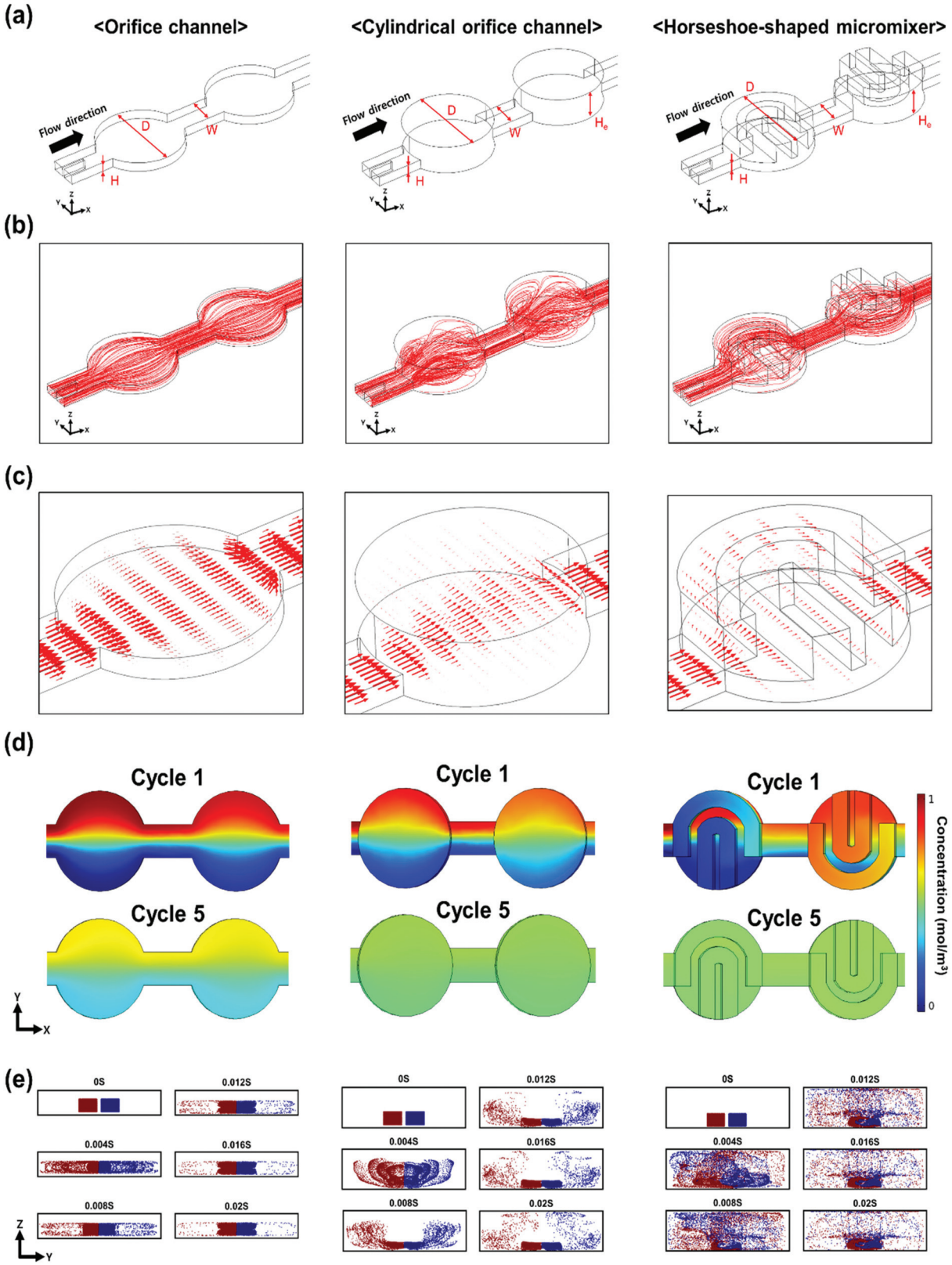

Fig. 2 Computational analysis of fluid mixing and particle movements in three different types of microfluidic channels. (a) 3D views of orifice channel (OC), cylindrical orifice channel (COC), and horseshoe-shaped micromixer (HOMM). (b) 3D views of streamlines following fluid velocity distribution. (c) 3D views of fluid distribution vectors in the channels. (d) Variations in two-fluid mixing with increasing number of cycles in each channel. (e) Cross-sectional views of particle movements over time.

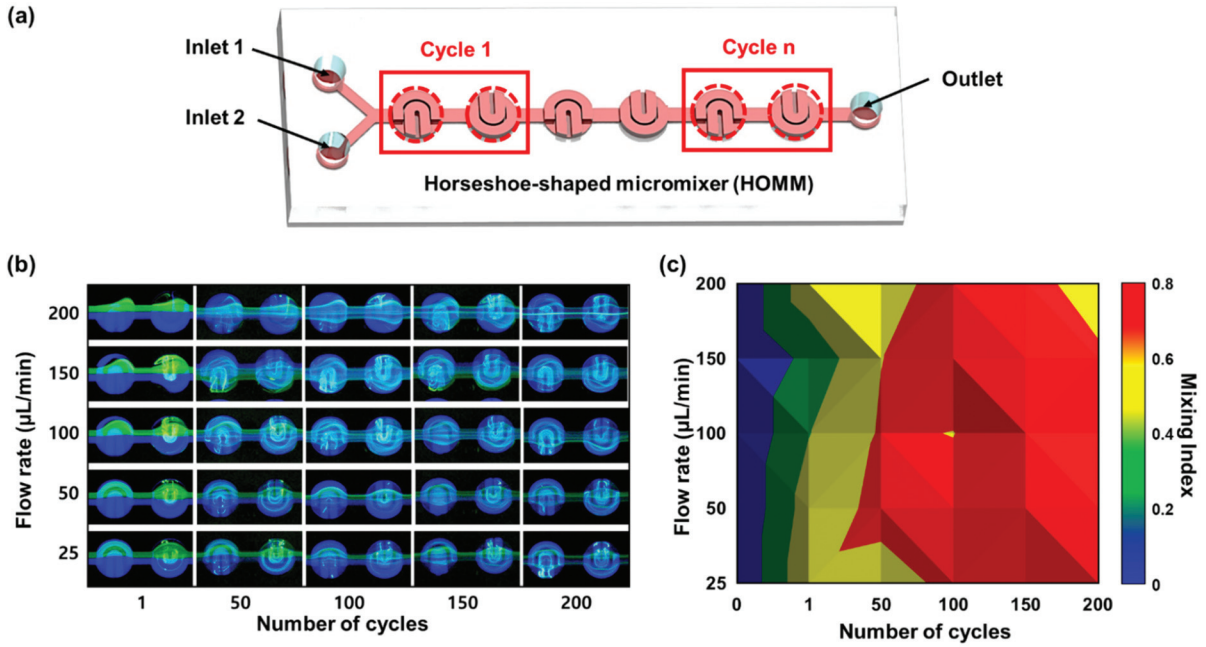

Fig. 3 Mixing indices (MIs) of micron-sized (microbeads) and nanosized particles (EVs) in the HOMM chip obtained for enhancing their collisions. (a) Schematic diagram of HOMM structures from cycles 1 to *n* assembled in an up–down format. (b) Images of 100 nm-sized (blue) and 7 μm-sized (green) fluorescent particles acquired for visualising and analysing particle distributions according to the cycles and flow rates in HOMM. (c) Effects of cycles and flow rates on MI in HOMM, with the minimum and maximum MIs being 0 and 1, respectively.

The maximum binding capacity per bead was estimated using the entire surfaces of the bead and EVs, and was calculated to be 1.6×10^4 EVs for the 7 μm-sized bead. The number of 100 μL microbeads was 1×10^6, which can manage $10^{9\sim10}$ EVs in one experiment. The CD63-antibody-coated (Anti-CD63 antibody [MEM-259], Abcam) 7 μm-sized beads and ten-fold-diluted plasma were injected into inlets 1 and 2 of the HOMM. The number of EVs was measured by NTA before and after EV injection into the HOMM chip. The EV concentration increased to 12.37×10^9 mL^{-1} until cycle 150 and slightly reduced at cycle 200 (flow rate of 50 μL min^{-1}; Fig. 4a). Therefore, the number of cycles was fixed at 150, and the flow rate was adjusted in the range of 50–200 μL min^{-1} at intervals of 50 μL min^{-1}. The EV concentration was approximately $12.37 \pm 0.99 \times 10^9$ mL^{-1}, $12.03 \pm 0.23 \times 10^9$ mL^{-1}, $12.56 \pm 0.49 \times 10^9$ mL^{-1}, and $13.56 \pm 0.41 \times 10^9$ mL^{-1} at flow rates of 50, 100, 150, and 200 μL min^{-1}, respectively, as shown in Fig. 4b. As the results of NTA analysis, the binding performance was not affected by the flow rates.

An average of 97.18 ± 1.42% were captured on a logarithmic scale based on the initial value by the beads at all EV concentrations, as shown in Fig. 4c. The number of EVs captured on the beads were similar to that of EVs captured on the microbead surfaces labeled with an anti-CD63 antibody (Clone H5C6) and conjugated with PE-Cy7, which were prepared to analyze the CD63 expression level in EVs using an FACS LSR II flow cytometer (BD, NJ, USA). The positive population of EV-containing beads was 14.3 ± 0.2% in the batch process for 2 min; moreover, the average populations were 47.7 ± 1.1%, 58.7 ± 0.5%, 53.0 ± 1.2%, and 45.4 ± 3.4% at flow rates of 50, 100, 150, and 200 μL min^{-1}, respectively (Fig. 4d and Fig. S3†). The number of EV-captured beads was reduced at a flow rate of 50 μL min^{-1} owing to the lack of inertial forces; a decrease was also observed at a flow rate of 200 μL min^{-1} owing to the short collision time between the antibody-coated microbeads and EVs. Based on the results of the binding performance, the working flow rate was 100–150 μL min^{-1}.

3.4. Validation of the fish trap performance

The operating flow rates of the two channels in the module—the HOMM component for the effective association of the EVs and microbeads, and the fish trap unit for capturing the EV-carrying microbeads and eluting the EVs—had to be optimized. Each trapping area in the fish trap unit consisted of 10 rectangles arranged in a V shape. Each rectangular pillar was 40 μm in length, 20 μm in width, and 10 μm in height. The small gap of the square pillars in the capture area was 5 μm smaller than the diameter of one microbead, as shown in Fig. 5a. After accumulating in the capture area, the remaining beads move to the next area through the large 30 μm-sized gap of the pillars. The streamlines of the fluid in this area of the chip pass through the small and large gaps in the pillars. The streamlines changed after the microbead trapping, and the direction of the streamlines shifted to the subsequent capture, as shown in Fig. 5a (right).

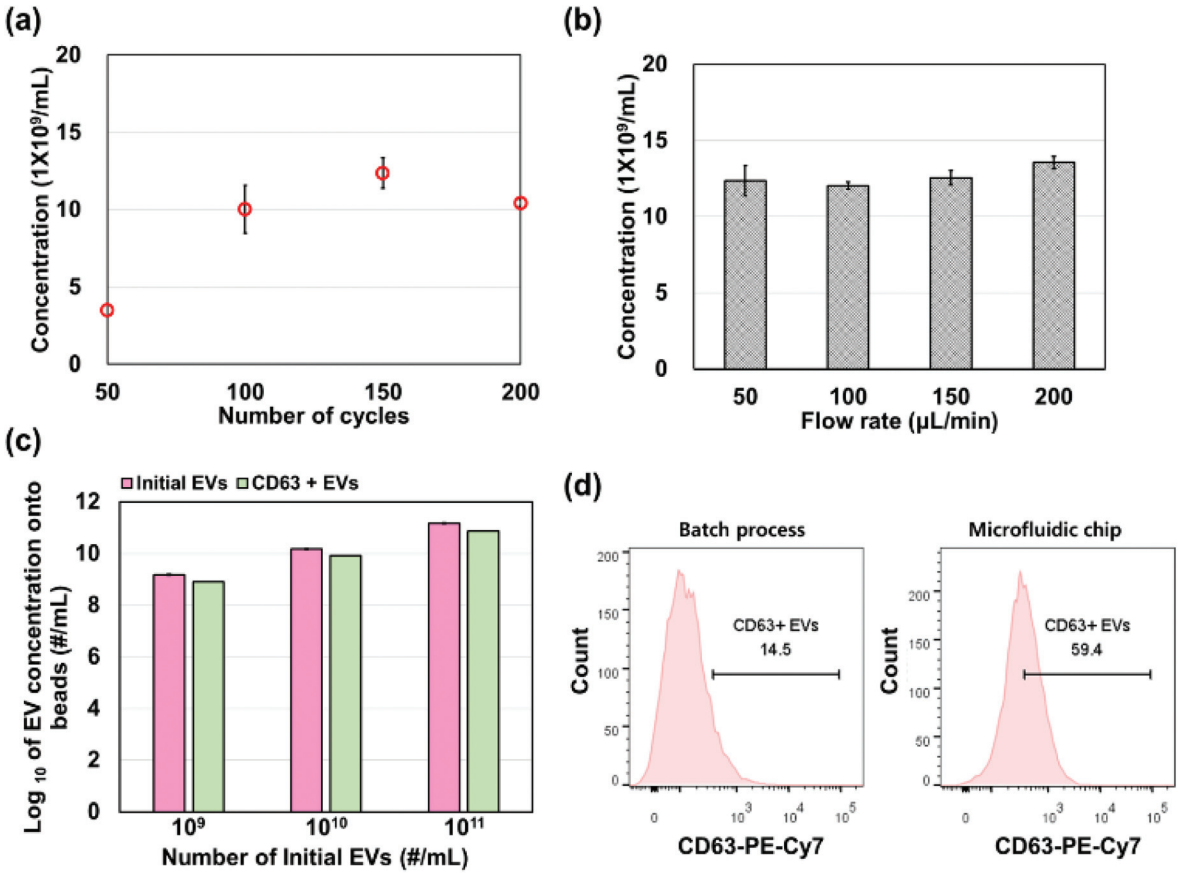

Fig. 4 Binding efficiency of EVs onto antibody-coated microbeads in HOMM. (a) Concentration of EVs bound to CD63-antibody-coated beads (7 μm) as a function of the number of cycles at a flow rate of 50 μL min^{-1}. (b) Concentration of EV-containing beads as a function of flow rate after 150 cycles of HOMM operation. (c) Concentration of bound EVs onto micro beads as a function of the number of EVs. (d) CD63-positive EVs on antibody-coated microbeads obtained by a batch process and the designed microfIfuidic chip analysed by FACS. Data are represented using average value (mean) ± standard deviation (n = 3).

Microbeads were loaded into the inlet of the fish trap unit and captured in the chip. The leftover beads were collected at the outlet using a haemocytometer. Thereafter, the binding efficiency was calculated as follows:

$$\text{Capture efficiency} = \left(1 - \frac{\text{number of microbeads in outlet}}{\text{number of microbeads in inlet}}\right) \times 100$$

Microbeads were injected into the fish trap chip at a flow rate of 50 μL min^{-1} depending on the bead concentration. As shown in Fig. 5b, the capture efficiency of the microbeads was almost 99.01 ± 0.33% at all concentrations. Therefore, the capture efficiency was not affected by the number of beads. Based on the conditions optimized for HOMM operation, an experiment on capturing microbeads was conducted at a bead concentration of 1×10^7 mL^{-1} in a flow rate range of 50–200 μL min^{-1}. The capture efficiency of the microbeads was approximately 98.02 ± 0.35% at flow rates of 50–150 μL min^{-1}. However, it decreased to 91.58 ± 0.97% at 200 μL min^{-1} in Fig. 5c. The inertial force of microbeads increases at a high flow rate and affects the capture efficiency because the inertial force varies primarily with respect to the microbead size and flow rate. An image of the captured microbeads was obtained using a camera (Progress Gryphax® Arktur, Jenopick, Germany) and an inverted optical microscope (IX-70, Olympus, Japan), as shown in Fig. 5d.

A low-pH buffer was used to disrupt the EV–microbead interactions and release the affinity-induced captured EVs from the microbeads. The elution buffer was injected into the chip at various flow rates. The purified EV concentrations at the outlet were 1.19 ± 0.22 × 10^8 mL^{-1}, 1.41 ± 0.14 × 10^8 mL^{-1}, 1.08 ± 0.07 × 10^8 mL^{-1}, 2.89 ± 0.12 × 10^8 mL^{-1}, and 2.62 ± 0.34 × 10^8 mL^{-1} at various flow rates from 6.25 μL min^{-1} to 100 μL min^{-1}. The largest amount of EVs was collected at the outlet at a flow rate of 50 μL min^{-1}; therefore, this value was selected to elute the EVs (Fig. 5e).

3.5. Analysis of cellular uptake based on the target-specific EVs purified from the fish-trap chip

The EVs and antibody-coated microbeads were suspended in PBS. Two solutions were injected into each inlet of the HOMM chip, and the target EVs were captured onto the beads. The EV-carrying beads moved to the fish trap chip connected to

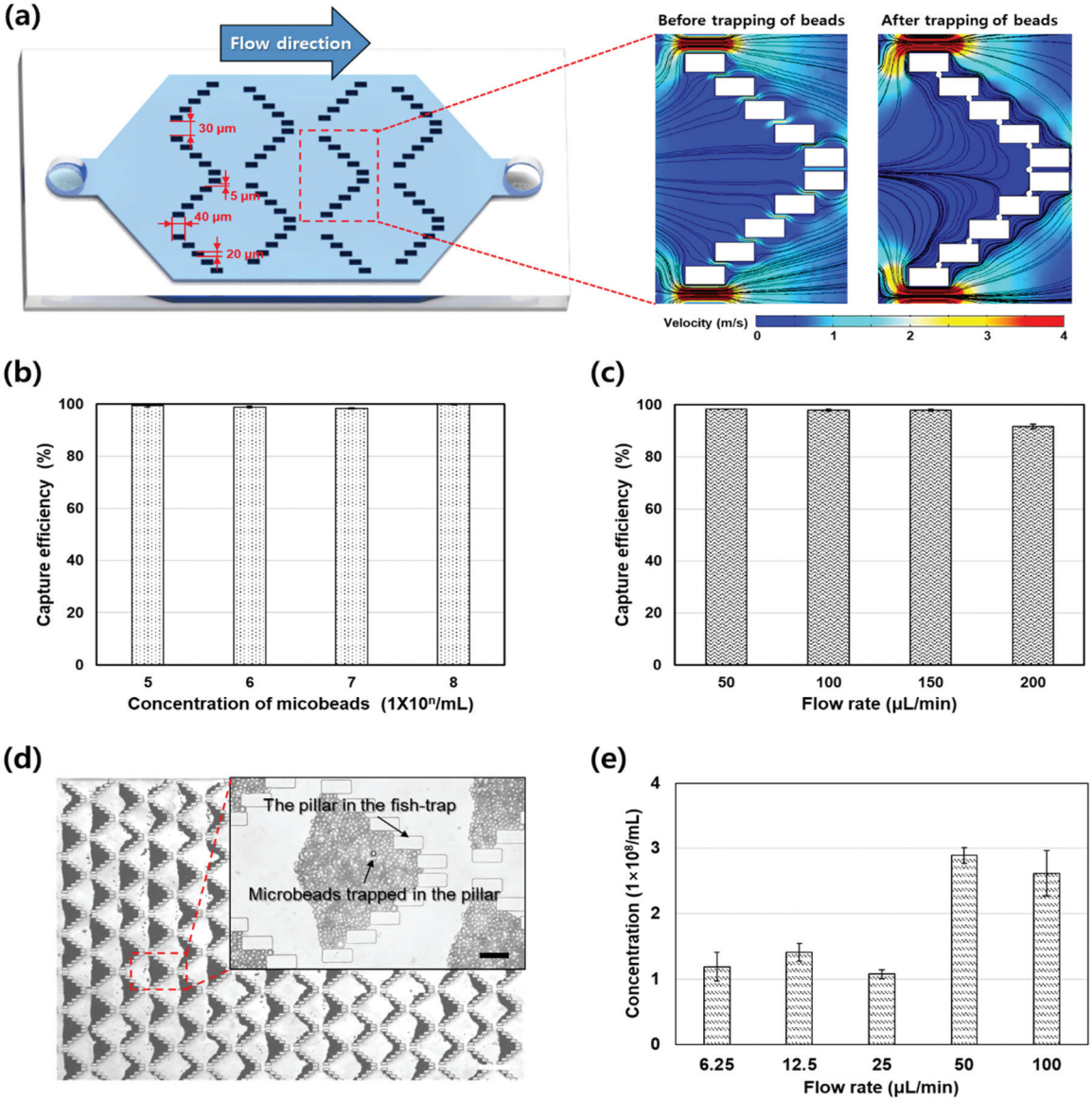

Fig. 5 (a) Top view and dimensions of the fish trap chip and the streamline variation of the chip before and after bead trapping. (b) Capture efficiency of microbeads by the chip depending on the microbead concentration. (c) Capture efficiencies of 1×10^7 mL^{-1} microbeads according to various flow rates. (d) Image of trapped microbeads in the chip (black and white scale bars represent 40 μm and 200 μm, respectively). (e) Dependence of isolated EVs from the trapped microbeads on flow rate. Data are represented using average value (mean) ± standard deviation (n = 3).

the HOMM chip. EVs were eluted with 100 μL of 0.1 M glycine–HCl (pH = 3.0) at a flow rate of 50 μL min^{-1} and collected into a tube containing 2.5 μL of 1 M Tris–HCl (pH = 9.0; AMRESCO, USA) to neutralise the eluted EVs.

The target-specific EVs purified from the fish-trap chip can be subject to the recipient cells in order to evaluate the efficiency of cellular uptake *in vitro*.[36] For this purpose, a specific target biomarker, PD-L1 had to be employed and it functions as an immune evasion to immune cells in the tumor microenvironment.[37,38] PD-L1 specific exosomes have higher metastatic features, compared with the total exosomes in cancer cells.[37,39] Therefore, the binding capability of specific PD-L1 EVs on the cancer cells was investigated to judge their cellular uptake as immune cells are important to monitoring the therapy response of cancer. To address this issue, the representative high PD-L1 expressing cancerous cell line (*i.e.* MDA-MB-231 cell) was used in our assay.[37] MDA-MB-231, is a triple-negative subtype of breast cancer. It is a highly heterogeneous tumor type with diverse biological behavior and results in the worst clinical outcome among the other subtypes of breast cancer. Since the MDA-MB-231 is used for an adequate *in vitro* model of interaction with T cell, which has PD-1, PD-L1 specific EVs from MDA-MB-231 can be also affected to T cells.

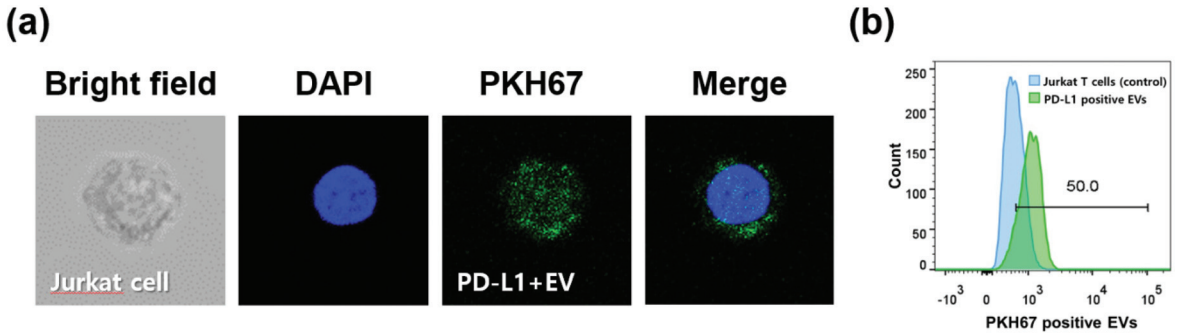

Fig. 6 (a) Confocal fluorescence microscopy images showing uptake of EVs from MDA-MB-231 cell culture media into Jurkat cells. The Jurkat cell and EVs stained by DAPI and PKH67 are indicated by the green fluorescence. (b) Flow cytometry analysis of the EVs and Jurkat T Cells. Moreover, the uptake of PKH67-labeled EVs (green) into Jurkat T cells (blue) is revealed.

Table 1 Comparison of the performance (processing time, capture efficiency, and sample volume) of EV capture and isolation technique

	Flow rate (μL min^{-1})	Capture efficiency (%)	Processing time (min)	Sample type	Ref.
HOMM & fish trap chip	100	97.2	5	Plasma media	This assay
OncoBean chip	50	—	60	Plasma media	32
Morpho butterfly wing-integratd microvertex biochip	1.6	75.2	~20	—	31

As proof of concept, it has been observed that the PD-L1 specific EVs from the cancer cell were adequately captured on the microbead surfaces and subsequently released through the fish trap chip. The PD-L1 EVs were then co-cultured with the representative recipient T cells (Jurkat cells) for 12 h, which was a suitable time for the recipient cell and specific EV interaction (Fig. 6a).

Next, the contents of the PD-L1 EVs surface marker bound on the Jurkat T cells were examined by flow cytometry and compared to Jurkat T cells without the EVs as a control. The Jurkat T cells co-cultured with PD-L1 EVs showed 50% of higher expression than the control cells (Fig. 6b), reflecting that the Jurkat T cells could successfully uptake the PD-L1 EVs purified by our chip. Consequently, this study provides the visual and quantitative evidence of cellular uptake *in situ* between tumor-specific EVs and recipient immune cells, indicating the availability of our integrated microfluidic chip.

4. Conclusion

The unique feature of the modular microfluidic platform described herein is the integration of two different microchips for the enrichment and isolation of target-specific EVs. These goals were realized as follows: (I) the HOMM unit selectively captured target EVs directly from cell culture media within 2 min; (II) the fish trap unit enriched the EVs and continuously released them from the microbeads; and (III) the entire device operation for EV enrichment and isolation was completed only in 5 min at a flow rate of 100 μL min^{-1}. The target EVs were readily and rapidly collected because of the use of only beads and the microfluidic device for EV enrichment and isolation.

Notably, in this study, the performance (processing time, capture efficiency, and sample volume) of our device is much better than other methods as shown in Table 1. The capture efficiency of EVs was 97.18% ± 1.42% and the total processing time was 5 min for 100 μL sample.

Moreover, the designed microfluidic chips can be used individually or collectively depending on the clinical requirement. For diagnostic applications, the EVs concentrated on the carrier beads by the HOMM chip operation alone can be analyzed by fluorescence-activated cell sorting (FACS) to measure the amount of EVs and their surface protein expression. Moreover, various approaches such as polymerase chain reaction (PCR) and western blotting (WB) can be exploited to investigate the cargo of EVs through the lysis of the EV-containing carrier beads. The pure EVs harvested by connecting the HOMM and fish trap chips enable their use in therapeutic tools such as medicines based on their own functions or *via* engineering of the internal and external transport.

Author contributions

Mr Hogyeong Gwak performed most experiments and wrote the manuscript. Professor Sunyoung Park contributed to the design of the study and assisted in writing the manuscript. Ms Haeun Yu performed some experiments and assisted in analysis of data. Professors Kyung-A Hyun and Hyo-Il Jung conceived and supervised the study. All authors were involved with designing the experiments and reviewing and discussing the data.

Conflicts of interest

There are no conflicts to declare.

Acknowledgements

This work was supported by the Technology Innovation Program (20008829) funded by the Ministry of Trade, Industry & Energy (MOTIE, Korea) (20008829), 2021Research Program through the National Research Foundation of Korea (NRF) funded by the Ministry of Science, ICT & Future Planning (2021R1C1C2007646), and the National Research Foundation of Korea (NRF) grant funded by the Korea government (MSIT) (No. 2020M3A9I4039045 and No. 2021R1A2C301125411).

References

1 R. Kalluri and V. S. LeBleu, *Science*, 2020, **367**, 1–15.
2 S. Keerthikumar, D. Chisanga, D. Ariyaratne, H. Saffar, S. Anand, K. N. Zhao, M. Samuel, M. Pathan, M. Jois, N. Chilamkurti, L. Gangoda and S. Mathivanan, *J. Mol. Biol.*, 2016, **428**, 688–692.
3 G. Raposo and W. Stoorvogel, *J. Cell Biol.*, 2013, **200**, 373–383.
4 Y. S. Ouyang, A. Bayer, T. J. Chu, V. A. Tyurin, V. E. Kagan, A. E. Morelli, C. B. Coyne and Y. Sadovsky, *Placenta*, 2016, **47**, 86–95.
5 S. Wang, Y. H. Dong, A. J. Gong, H. M. Kong, J. N. Gao, X. D. Hao, Y. M. Liu, Z. B. Wang, Y. Q. Fan, C. Y. Liu and W. H. Xu, *Int. J. Biol. Sci.*, 2021, **17**, 562–573.
6 A. Conigliaro and C. Cicchini, *J. Clin. Med.*, 2019, **8**, 1–17.
7 L. Mashouri, H. Yousefi, A. R. Aref, A. M. Ahadi, F. Molaei and S. K. Alahari, *Mol. Cancer*, 2019, **18**, 1–14.
8 H. Gwak, S. Park, J. Kim, J. D. Lee, I. S. Kim, S. I. Kim, K. A. Hyun and H. I. Jung, *Biosens. Bioelectron.*, 2021, **192**, 1–9.
9 M. W. Kim, S. Park, H. Lee, H. Gwak, K. A. Hyun, J. Y. Kim, H. I. Jung and S. I. Kim, *Cancer Sci.*, 2021, **112**, 5078–5087.
10 N. A. Hanjani, *et al.*, *Crit. Rev. Oncol. Hematol.*, 2022, **169**, 103565.
11 J. De Toro, L. Herschlik, C. Waldner and C. Mongini, *Front. Immunol.*, 2015, **6**, 1–12.
12 A. Moller and R. J. Lobb, *Nat. Rev. Cancer*, 2020, **20**, 697–709.
13 R. Xu, A. Rai, M. S. Chen, W. Suwakulsiri, D. W. Greening and R. J. Simpson, *Nat. Rev. Clin Oncol.*, 2018, **15**, 617–638.
14 M. P. Zaborowski, L. Balaj, X. O. Breakefield and C. P. Lai, *Bioscience*, 2015, **65**, 783–797.
15 C. Thery, K. W. Witwer, E. Aikawa, M. J. Alcaraz, J. D. Anderson, R. Andriantsitohaina, A. Antoniou, T. Arab, F. Archer, G. K. Atkin-Smith, D. C. Ayre, J. M. Bach, D. Bachurski, H. Baharvand, L. Balaj, S. Baldacchino, N. N. Bauer, A. A. Baxter, M. Bebawy, C. Beckham, A. B. Zavec, A. Benmoussa, A. C. Berardi, P. Bergese, E. Bielska, C. Blenkiron, S. Bobis-Wozowicz, E. Boilard, W. Boireau, A. Bongiovanni, F. E. Borras, S. Bosch, C. M. Boulanger, X. Breakefield, A. M. Breglio, M. A. Brennan, D. R. Brigstock, A. Brisson, M. L. D. Broekman, J. F. Bromberg, P. Bryl-Gorecka, S. Buch, A. H. Buck, D. Burger, S. Busatto, D. Buschmann, B. Bussolati, E. I. Buzas, J. B. Byrd, G. Camussi, D. R. F. Carter, S. Caruso, L. W. Chamley, Y. T. Chang, C. C. Chen, S. Chen, L. Cheng, A. R. Chin, A. Clayton, S. P. Clerici, A. Cocks, E. Cocucci, R. J. Coffey, A. Cordeiro-da-Silva, Y. Couch, F. A. W. Coumans, B. Coyle, R. Crescitelli, M. F. Criado, C. D'Souza-Schorey, S. Das, A. D. Chaudhuri, P. de Candia, E. F. De Santana, O. De Wever, H. A. del Portillo, T. Demaret, S. Deville, A. Devitt, B. Dhondt, D. Di Vizio, L. C. Dieterich, V. Dolo, A. P. D. Rubio, M. Dominici, M. R. Dourado, T. A. P. Driedonks, F. V. Duarte, H. M. Duncan, R. M. Eichenberger, K. Ekstrom, S. E. L. Andaloussi, C. Elie-Caille, U. Erdbrugger, J. M. Falcon-Perez, F. Fatima, J. E. Fish, M. Flores-Bellver, A. Forsonits, A. Frelet-Barrand, F. Fricke, G. Fuhrmann, S. Gabrielsson, A. Gamez-Valero, C. Gardiner, K. Gartner, R. Gaudin, Y. S. Gho, B. Giebel, C. Gilbert, M. Gimona, I. Giusti, D. C. I. Goberdhan, A. Gorgens, S. M. Gorski, D. W. Greening, J. C. Gross, A. Gualerzi, G. N. Gupta, D. Gustafson, A. Handberg, R. A. Haraszti, P. Harrison, H. Hegyesi, A. Hendrix, A. F. Hill, F. H. Hochberg, K. F. Hoffmann, B. Holder, H. Holthofer, B. Hosseinkhani, G. K. Hu, Y. Y. Huang, V. Huber, S. Hunt, A. G. E. Ibrahim, T. Ikezu, J. M. Inal, M. Isin, A. Ivanova, H. K. Jackson, S. Jacobsen, S. M. Jay, M. Jayachandran, G. Jenster, L. Z. Jiang, S. M. Johnson, J. C. Jones, A. Jong, T. Jovanovic-Talisman, S. Jung, R. Kalluri, S. Kano, S. Kaur, Y. Kawamura, E. T. Keller, D. Khamari, E. Khomyakova, A. Khvorova, P. Kierulf, K. P. Kim, T. Kislinger, M. Klingeborn, D. J. Klinke, M. Kornek, M. M. Kosanovic, A. F. Kovacs, E. M. Kramer-Albers, S. Krasemann, M. Krause, I. V. Kurochkin, G. D. Kusuma, S. Kuypers, S. Laitinen, S. M. Langevin, L. R. Languino, J. Lannigan, C. Lasser, L. C. Laurent, G. Lavieu, E. Lazaro-Ibanez, S. Le Lay, M. S. Lee, Y. X. F. Lee, D. S. Lemos, M. Lenassi, A. Leszczynska, I. T. S. Li, K. Liao, S. F. Libregts, E. Ligeti, R. Lim, S. K. Lim, A. Line, K. Linnemannstons, A. Llorente, C. A. Lombard, M. J. Lorenowicz, A. M. Lorincz, J. Lotvall, J. Lovett, M. C. Lowry, X. Loyer, Q. Lu, B. Lukomska, T. R. Lunavat, S. L. N. Maas, H. Malhi, A. Marcilla, J. Mariani, J. Mariscal, E. S. Martens-Uzunova, L. Martin-Jaular, M. C. Martinez, V. R. Martins, M. Mathieu, S. Mathivanan, M. Maugeri, L. K. McGinnis, M. J. McVey, D. G. Meckes, K. L. Meehan, I. Mertens, V. R. Minciacchi, A. Moller, M. M. Jorgensen, A. Morales-Kastresana, J. Morhayim, F. Mullier, M. Muraca, L. Musante, V. Mussack, D. C. Muth, K. H. Myburgh, T. Najrana, M. Nawaz, I. Nazarenko, P. Nejsum, C. Neri, T. Neri, R. Nieuwland, L. Nimrichter, J. P. Nolan, E. N. M. Nolte-'t Hoen, N. Noren Hooten, L. O'Driscoll, T. O'Grady, A. O'Loghlen, T. Ochiya, M. Olivier, A. Ortiz,

L. A. Ortiz, X. Osteikoetxea, O. Ostegaard, M. Ostrowski, J. Park, D. M. Pegtel, H. Peinado, F. Perut, M. W. Pfaffl, D. G. Phinney, B. C. H. Pieters, R. C. Pink, D. S. Pisetsky, E. P. von Strandmann, I. Polakovicova, I. K. H. Poon, B. H. Powell, I. Prada, L. Pulliam, P. Quesenberry, A. Radeghieri, R. L. Raffai, S. Raimondo, J. Rak, M. I. Ramirez, G. Raposo, M. S. Rayyan, N. Regev-Rudzki, F. L. Ricklefs, P. D. Robbins, D. D. Roberts, S. C. Rodrigues, E. Rohde, S. Rome, K. M. A. Rouschop, A. Rughetti, A. E. Russell, P. Saa, S. Sahoo, E. Salas-Huenuleo, C. Sanchez, J. A. Saugstad, M. J. Saul, R. M. Schiffelers, R. Schneider, T. H. Schoyen, A. Scott, E. Shahaj, S. Sharma, O. Shatnyeva, F. Shekari, G. V. Shelke, A. K. Shetty, K. Shiba, P. R. M. Siljander, A. M. Silva, A. Skowronek, O. L. Snyder, R. P. Soares, B. W. Sodar, C. Soekmadji, J. Sotillo, P. D. Stahl, W. Stoorvogel, S. L. Stott, E. F. Strasser, S. Swift, H. Tahara, M. Tewari, K. Timms, S. Tiwari, R. Tixeira, M. Tkach, W. S. Toh, R. Tomasini, A. C. Torrecilhas, J. P. Tosar, V. Toxavidis, L. Urbanelli, P. Vader, B. W. M. van Balkom, S. G. van der Grein, J. Van Deun, M. J. C. van Herwijnen, K. Van Keuren-Jensen, G. van Niel, M. E. van Royen, A. J. van Wijnen, M. H. Vasconcelos, I. J. Vechetti, T. D. Veit, L. J. Vella, E. Velot, F. J. Verweij, B. Vestad, J. L. Vinas, T. Visnovitz, K. V. Vukman, J. Wahlgren, D. C. Watson, M. H. M. Wauben, A. Weaver, J. P. Webber, V. Weber, A. M. Wehman, D. J. Weiss, J. A. Welsh, S. Wendt, A. M. Wheelock, Z. Wiener, L. Witte, J. Wolfram, A. Xagorari, P. Xander, J. Xu, X. M. Yan, M. Yanez-Mo, H. Yin, Y. Yuana, V. Zappulli, J. Zarubova, V. Zekas, J. Y. Zhang, Z. Z. Zhao, L. Zheng, A. R. Zheutlin, A. M. Zickler, P. Zimmermann, A. M. Zivkovic, D. Zocco and E. K. Zuba-Surma, *J. Extracell. Vesicles*, 2018, **7**, 1–43.

16 C. Thery, S. Amigorena, G. Raposo and A. Clayton, *Curr. Protoc. Cell Biol.*, 2006, **30**, 3–22.

17 K. W. Witwer, E. I. Buzas, L. T. Bemis, A. Bora, C. Lasser, J. Lotvall, E. N. Nolte-'t Hoen, M. G. Piper, S. Sivaraman, J. Skog, C. Thery, M. H. Wauben and F. Hochberg, *J. Extracell. Vesicles*, 2013, **2**, 1–25.

18 Y. Yoshioka, N. Kosaka, Y. Konishi, H. Ohta, H. Okamoto, H. Sonoda, R. Nonaka, H. Yamamoto, H. Ishii, M. Mori, K. Furuta, T. Nakajima, H. Hayashi, H. Sugisaki, H. Higashimoto, T. Kato, F. Takeshita and T. Ochiya, *Nat. Commun.*, 2014, **5**, 1–8.

19 S. Kamerkar, V. S. LeBleu, H. Sugimoto, S. J. Yang, C. F. Ruivo, S. A. Melo, J. J. Lee and R. Kalluri, *Nature*, 2017, **546**, 498–503.

20 D. D. Taylor and C. Gercel-Taylor, *Semin. Immunopathol.*, 2011, **33**, 441–454.

21 Y. J. Chiu, W. Cai, Y. R. V. Shih, I. Lian and Y. H. Lo, *Small*, 2016, **12**, 3658–3666.

22 C. Chen, J. Skog, C. H. Hsu, R. T. Lessard, L. Balaj, T. Wurdinger, B. S. Carter, X. O. Breakefield, M. Toner and D. Irimia, *Lab Chip*, 2010, **10**, 505–511.

23 R. T. Davies, J. Kim, S. C. Jang, E. J. Choi, Y. S. Gho and J. Park, *Lab Chip*, 2012, **12**, 5202–5210.

24 Z. X. Wang, H. J. Wu, D. Fine, J. Schmulen, Y. Hu, B. Godin, J. X. J. Zhang and X. W. Liu, *Lab Chip*, 2013, **13**, 2879–2882.

25 K. Lee, H. L. Shao, R. Weissleder and H. Lee, *ACS Nano*, 2015, **9**, 2321–2327.

26 H. L. Shao, J. Chung, K. Lee, L. Balaj, C. Min, B. S. Carter, F. H. Hochberg, X. O. Breakefield, H. Lee and R. Weissleder, *Nat. Commun.*, 2015, **6**, 1–9.

27 C. Liu, J. Y. Guo, F. Tian, N. Yang, F. S. Yan, Y. P. Ding, J. Y. Wei, G. Q. Hu, G. J. Nie and J. S. Sun, *ACS Nano*, 2017, **11**, 6968–6976.

28 C. L. Hisey, K. D. P. Dorayappan, D. E. Cohn, K. Selvendiran and D. J. Hansford, *Lab Chip*, 2018, **18**, 3144–3153.

29 Y. T. Kang, E. Purcell, T. Hadlock, T. W. Lo, A. Mutukuri, S. Jolly and S. Nagrath, *Analyst*, 2019, **144**, 5785–5793.

30 P. Zhang, X. Zhou, M. He, Y. Q. Shang, A. L. Tetlow, A. K. Godwin and Y. Zeng, *Nat. Biomed. Eng.*, 2019, **3**, 438–451.

31 S. Y. Han, Y. S. Xu, J. Sun, Y. F. Liu, Y. J. Zhao, W. G. Tao and R. J. Chai, *Biosens. Bioelectron.*, 2020, **154**, 1–9.

32 T. W. Lo, Z. W. Zhu, E. Purcell, D. Watza, J. Wang, Y. T. Kang, S. Jolly, D. Nagrath and S. Nagrath, *Lab Chip*, 2020, **20**, 1762–1770.

33 S. Hossain, M. A. Ansari, A. Husain and K. Y. Kim, *Chem. Eng. J.*, 2010, **158**, 305–314.

34 S. Hossain and K. Y. Kim, *SpringerPlus*, 2016, **5**, 1–16.

35 Y. Z. Liu, B. J. Kim and H. J. Sung, *Int. J. Heat Fluid Flow*, 2004, **25**, 986–995.

36 M. Mathieu, L. Martin-Jaular, G. Lavieu and C. Thery, *Nat. Cell Biol.*, 2019, **21**, 9–17.

37 Y. F. Qiu, Y. Yang, R. Y. Yang, C. X. Liu, J. M. Hsu, Z. Jiang, L. L. Sun, Y. K. Wei, C. W. Li, D. H. Yu, J. Zhang and M. C. Hung, *Oncogene*, 2021, **40**, 4992–5001.

38 Y. H. Shi, J. H. Zhang, Z. Y. Mao, H. Jiang, W. Liu, H. Shi, R. B. Ji, W. R. Xu, H. Qian and X. Zhang, *Front. Oncol.*, 2020, **10**, 1–9.

39 G. Chen, A. C. Huang, W. Zhang, G. Zhang, M. Wu, W. Xu, Z. L. Yu, J. G. Yang, B. K. Wang, H. H. Sun, H. F. Xia, Q. W. Man, W. Q. Zhong, L. F. Antelo, B. Wu, X. P. Xiong, X. M. Liu, L. Guan, T. Li, S. J. Liu, R. F. Yang, Y. T. Lu, L. Y. Dong, S. McGettigan, R. Somasundaram, R. Radhakrishnan, G. Mills, Y. L. Lu, J. Kim, Y. H. H. Chen, H. D. Dong, Y. F. Zhao, G. C. Karakousis, T. C. Mitchell, L. M. Schuchter, M. Herlyn, E. J. Wherry, X. W. Xu and W. Guo, *Nature*, 2018, **560**, 382–386.